Journal of
MATERIALS RESEARCH

Article
DOI:10.1557/s43578-023-01027-4

The influence of the mixed phase (Ti–TiO_2(A): TiO_2(R)) on the optical band gap of TiO_2 nanotubes heat treated at different temperatures

D. Zalouk[1,2,a)], D. Hatem[2], D. Hocine[2], M. S. Belkaid[2], T. Hadjersi[3], Y. Kebbati[4], S. Boudinar[5]
[1] *URMPE, University M'Hamed Bougara, 35000 Boumerdes, Algeria*
[2] *LATAGE, University Mouloud Mammeri, BP 17 RP, 15000 Tizi-Ouzou, Algeria*
[3] *CRTSE 02, Bd Frantz Fanon, BP. 140, Merveilles, Algeria*
[4] *Laboratory of Physics and Chemistry of the Environment and Space LPC2E, University of Orléans, Orléans, France*
[5] *LPCM, University Mouloud Mammeri, BP17 RP, 15000 Tizi-Ouzou, Algeria*
[a)] Address all correspondence to this author. e-mail: D.zalouk@yahoo.fr

Received: 5 November 2022; accepted: 1 May 2023

Highly ordered TiO_2 nanotubes (NTs) were synthesized by electrochemical anodization than annealed at different temperatures between 300 and 900 °C for 3 h. The elaborated NTs adhere well to the Ti substrate over the annealing temperature range of 300–600 °C. The TiO_2 NTs morphology begins to gradually evolve for temperatures up to 700 °C and approaches that of nanoparticles until the latter become predominant at T above 800 °C. Reflection measurements show that the NTs present reflection of 7% at 600 °C, corresponding to the lowest band gap 2.59 eV. This can be related to the presence of the mixed phase (Ti–$TiO_{2(A)}$–$TiO_{2(R)}$).The charge carrier density decreases from $2.34 \times 10^{+21}$ to $3.61 \times 10^{+13}$ $cm^{-3}$when the annealing temperature increases, that accompanied by a reduction in the resistivity from 142.23 to 29.56Ω.cm which is adequate to photo anode application.

Introduction

In the recent years, nanomaterials attracted much interest due to their excellent properties that allow them to be used in various applications [1–10]. Among them, we find the titanium dioxide and the TiO_2 nanotubes (TNTs) which are the most important nanomaterials owing to their large specific surface area, low charge carriers recombination, interesting properties such as efficient conduction of electrons [11–17], excellent mechanical strength, and highly oriented tubular structure. Thanks to these properties, TiO_2 nanotubes can be used in numerous applications such as photovoltaic cells [18], photocatalysis [19], water photoelectrolysis [20], Li-batteries [21], gas sensor [22]. Moreover, they have been investigated for DRAM (Dynamic Random Access Memory) applications due to their high dielectric constant and chemical and thermal stability [23–25].

TiO_2 is an *n*-type semiconductor having several crystal structures especially the anatase, rutile, and brokite phases [26]. The anatase phase is obtained at temperatures below 600 °C, which is suitable for applications such as solar cells and photocatalysis while the rutile phase is dynamically stable at temperatures above 600 °C [27], which are used in photoelectrochemistry and as a white pigment [28] in cosmetics due to its efficient light scattering.

Additionally, it is well established that as-synthesized nanotubes are amorphous [29, 30], and crystallizes after an annealing treatment. Indeed, amorphous phase transition to anatase crystalline phase begins at a 280 °C temperature [31], while anatase to rutile crystalline phases transition occurs in the range of 500–1000 °C. This transition is more related to the presence of impurities, size, shape, and experimental parameters for the synthesis of nanostructures [31, 32].

Various methods are used for the synthesis of titanium nanotubes namely the template-assisted [33] as well as electrochemical anodization [34] and hydrothermal [35]. Since that Grimes [36] shown the electrochemical anodization method allows to synthesis highly ordered and vertically oriented TiO_2 nanotube arrays, it becomes a universal and effective preparation method. For these reasons and due to its simplicity, the anodization method was employed in this work to grow the TiO_2 nanotubes.

Obviously, to apply TiO_2 nanotubes at different temperatures, it was first necessary to know its thermal properties. Although some studies assume phase stability up to 400 °C [37, 38], other results, on the other hand, do not allow to conclude on its structural stability at high temperature [37–39].

It should be mentioned that in most of the previous work dealing with TiO_2 nanotubes prepared via the electrochemical anodization method, the annealing temperature is a key parameter to control the phase transition in TiO_2 nanotubes structures which is interesting essentially in photovoltaic applications. In fact, the efficiency of dye sensitized solar cell (DSSC) increased by mixing TiO_2 phases [40, 41].

Therefore, it is very interesting to investigate phase transition and correlates them with the physical properties of TiO_2 nanotubes. It is in this context that our contribution takes place. Indeed, this work aimed to develop a mixture phases to reduce the band gap of nanotubular TiO_2. We opted for a heat treatment of our samples in the range of 300–900°C. Compared to other methods already used for the reduction of the optical band gap of TiO_2, such as the doping technique [42–47], heat treatment is an alternative, simple, less expensive, non-toxic method, and can be easily implemented. Recently, it is shown that the optimization of annealing profile and temperature lead to considerable enhancement on the TiO_2 properties [48–50]. Depending on the properties of TiO_2 obtained, several fields of application will be possible such as DSSC, hybrid, perovskite solar cells, and photocatalysis. The improvement of the properties of nanotubular titanium dioxide (TiO_2) allows increasing the efficiency of the photo-anodes manufactured using this material by improving simultaneously the photo absorption as well as the process of charge transfer.

The evolution of optical, morphological, and structural properties of TiO_2 nanotubes were studied, respectively, by the diffuse reflectance spectroscopy, scanning electron microscopy (SEM), and X-ray diffraction (XRD). The electronic density of TiO_2 nanotubes was determined by electrochemical impedance spectroscopy (Mott-Schottky plot) and the electrical resistivity measurement of TiO_2 nanotubes was carried out using the four points probe.

Results and discussion

EDX analysis of TiO_2 nanotubes

Figure 1 displays the plan view SEM image and tilted of thermally untreated titanium nanotubes (TNT) obtained by anodization at 50 V for 2 h. this figure reveals that the titanium nanotube arrays (TNTAs) are made up of highly ordered and aligned nanotubes. The nanotubes have a mean inner diameter, a wall thickness, and a length of, respectively, about 193 nm, 31 nm, and 2.15 µm as can be seen (Fig. 1a and b).

Chemical composition of titanium and titanium nanotube substrates was analyzed using the EDX technique. Figure 1(c) shows energy dispersive X-ray spectra of titanium substrate and TiO_2 nanotubes thermally treated at 500 °C for 3 h [Fig. 1(d)]. It shows that Ti foil is only composed of Ti [Fig. 1(c)], while TiO_2 nanotube substrate is constituted of Ti and O [Fig. 1(d)]. The latter result can indicate the formation of TiO_2 nanotubes. The absence of some undetectable elements coming from the electrolyte like sodium, fluorine, and hydrogen ions indicates a good rinsing with deionized water that was performed. It is difficult to determine the Ti/O concentration ratio due to the difficulty of precisely separated the O and Ti peaks located at 0.51 keV and 0.48 keV, respectively.

Effect of temperature on morphological structure of TiO_2 nanotube

To evaluate the influence of the thermally treatment temperature on the surface morphology of TiO_2 nanotubes, SEM observations were performed.

Figure 2 shows the evolution of the morphology of samples with the thermal treatment temperature from 200 to 1000 °C for 3 h. The SEM images show that the morphology of the TiO_2 nanotubes is clearly influenced by the annealing temperature, especially when crystallization is performed at $T \geq 700$ °C [Fig. 2(f–i)]. Indeed, it can be noted that annealing at temperatures in the range of 200–600 °C doesn't lead to significant change except that the walls of tubes become thinner [Fig. 2(a–e)]. However, at annealing temperatures upper than 700 °C, the morphology significantly change so that the nanotubes collapse from 800 °C as can be seen in the [Fig. 2(g–i)]. These results are very important since the tubular form were successfully kept until temperatures as higher as 600 °C. Indeed, Jaroenworaluck et al. observed that TiO_2 nanotubes collapse after annealing at 500–600 C [51]. Also Pham Van Viet et al., shows that the titanium nanotubes still keep a tubular morphology at 300 °C and they undergo gradual change into nanoparticles, which disappear completely in the range of 400–500 °C [52]. Scheme 1 shows the change in theTiO_2 nanotubes morphology with increasing temperature.

Raising the temperature further to 700 °C, the nanotubes became very fragmented, which is in agreement with the literature where it is stated that thermal treatment creates microscopic cracks in the films of the TiO_2 tubes [53–55] which leads to its taking off. After heat treatment of the detached layer of nanotubes at the temperature of 800 °C, the degradation caused by thermal cracking and collapsing of the tubes Fig. 2(g), indicating the limiting of thermal stability at this temperature.

From Fig. 2(h), it can be observed that the nanotubes were completely degraded after thermal treatment at 900 °C. They are melted into nanoparticles [56, 57] with a diameter between 80

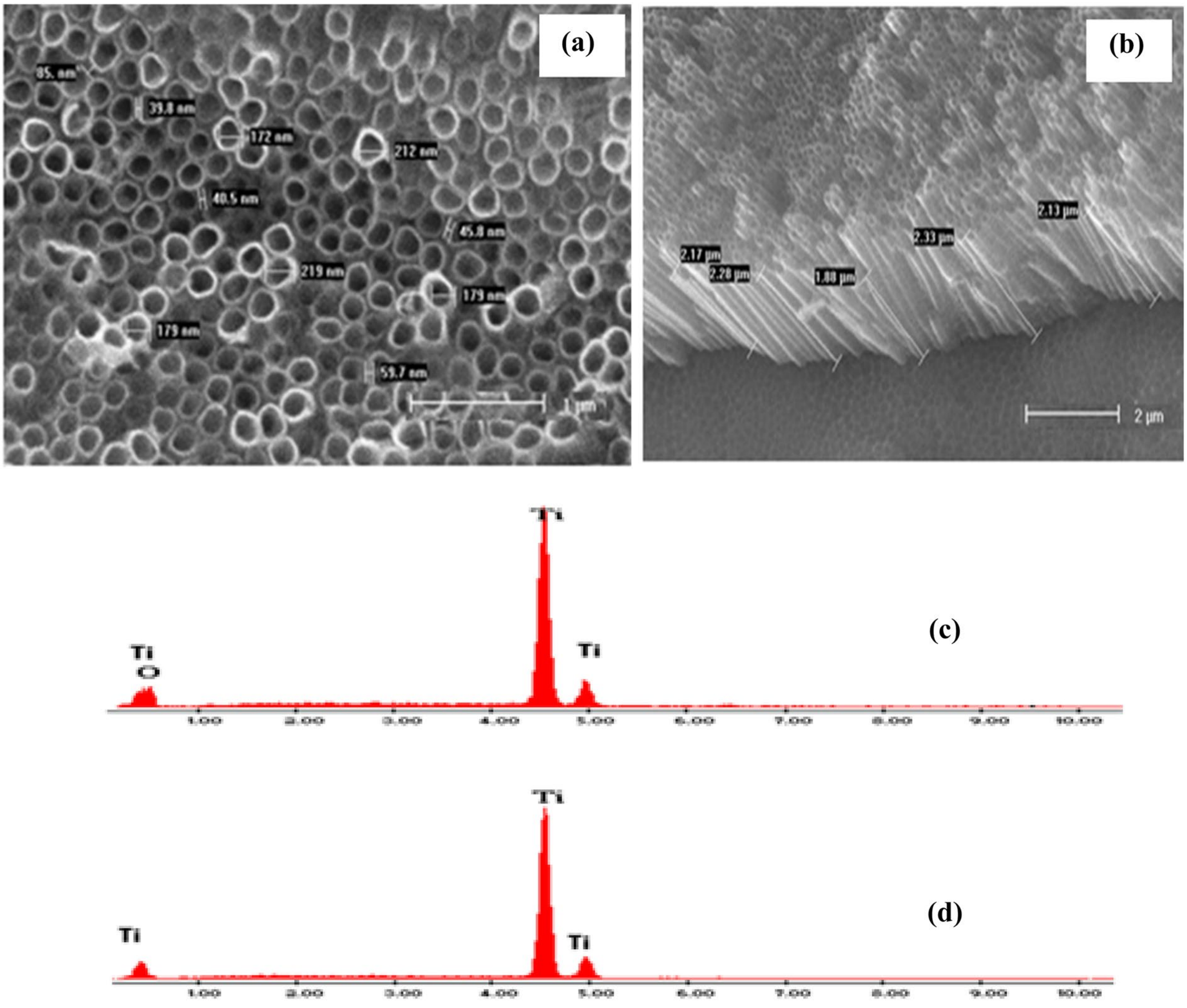

Figure 1: (a) Plan and (b) tilted view SEM images of TiO_2 nanotubes obtained by anodization at 50 V for2 h in an ethylene glycol solution and EDX spectra of: (c) Ti substrate, (d) substrate of TiO_2 nanotubes annealed at 500 °C for 3 h.

and 349 nm. Above 900 °C, the TiO_2 nanotubes layer becomes in the form of a porous powder. The size of these nanoparticles decreases by rising the temperature from 900 to 1000 °C as can be seen in [Figs. 2(h and i)].

X-ray diffraction (XRD) studies

To clarify the influence of thermal treatment temperature on the structural propriety of TiO_2 nanotubes, the XRD technique was used to identify and determine the phase structure and the crystallite size for each annealing temperature. Figure 3 compares the XRD patterns of TiO_2 nanotubes arrays sintered in air for 3 h at various temperatures: 300, 400, 500, 600, 700, 800, and 900 °C. The diffractogram of TiO_2 nanotubes without annealing was also obtained which was used as reference.

It can be observed that the XRD diffractograms of sample annealed at 300 and 400 °C, exhibit only diffraction peaks of titanium substrate, indicating that the TiO_2 crystalline phases don't formed. This does not eliminate the possibility of formation of the TiO_2 amorphous phase, i.e., TiO_2 nanotubes; this to be consistent with the SEM results [58–64]. At higher annealing temperatures, the XRD patterns reveal the presence of characteristics peak of anatase and rutile phases. However, the peaks corresponding to anatase phase disappear at temperatures above 600 °C. These results allow to suggest that the titanium nanotubes start to crystallize from the thermal treatment temperature of 500 °C with a anatase phase, this because of apparition of peaks at $2\theta = 25°$. However, At 600 °C the XRD shows the presence of a small portion of the rutile phase in addition to a Ti phase (Ti–TiO_2(A)–TiO_2(R)) (Fig. 3). After annealing at 700 °C, all TiO_2 nanotube structures are converted into a single-phase namely rutile. In addition, it can be seen that the Titanium diffraction peaks disappear at 800 °C. Overall; these results are in agreement with those of the literature. Indeed, it was reported

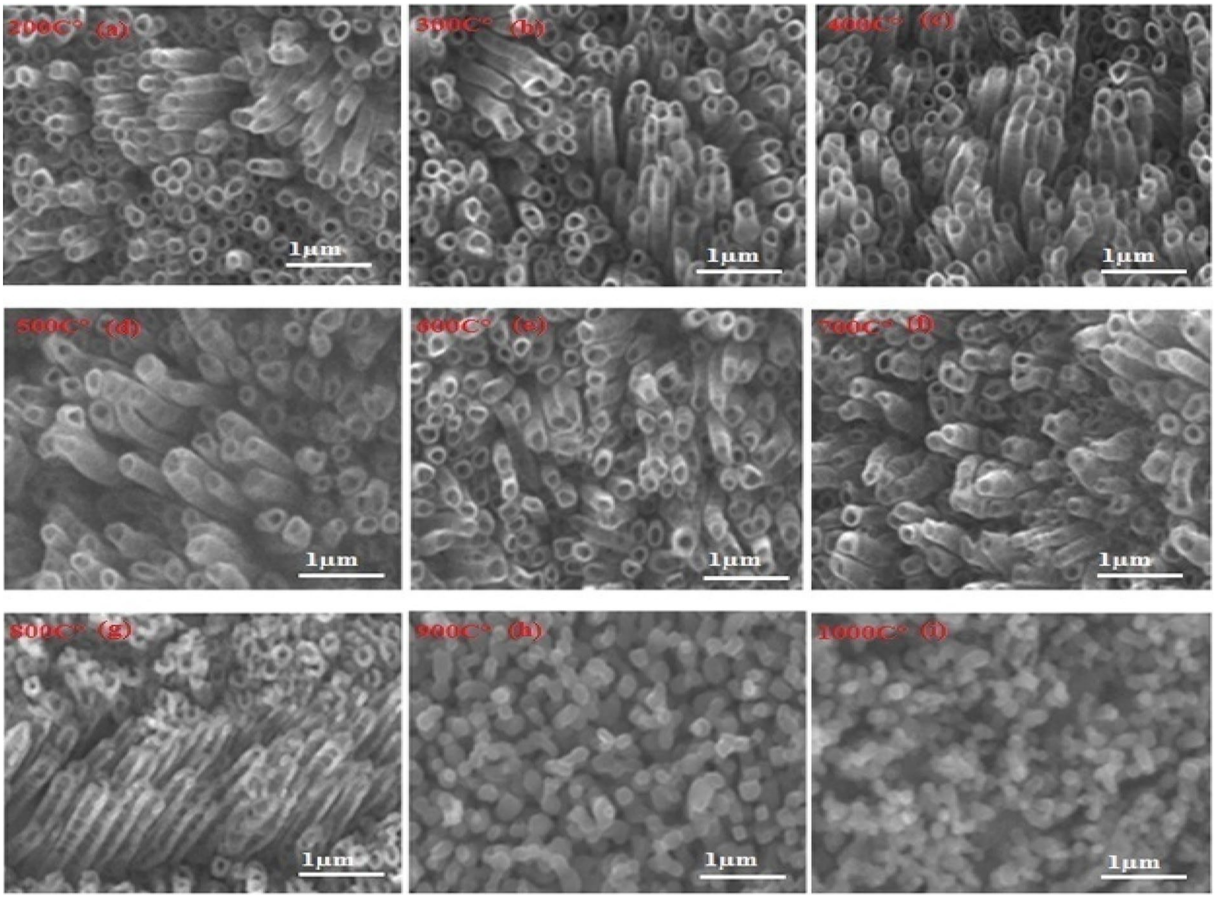

Figure 2: SEM images of TiO_2 nanotubes after annealed in air for 3 h at: (a) 200 °C, (b) 300 °C, (c) 400 °C, (d)500 °C, (e) 600 °C, (f) 700 °C, (g) 800 °C, (h) 900 °C, and (i)1000 °C.

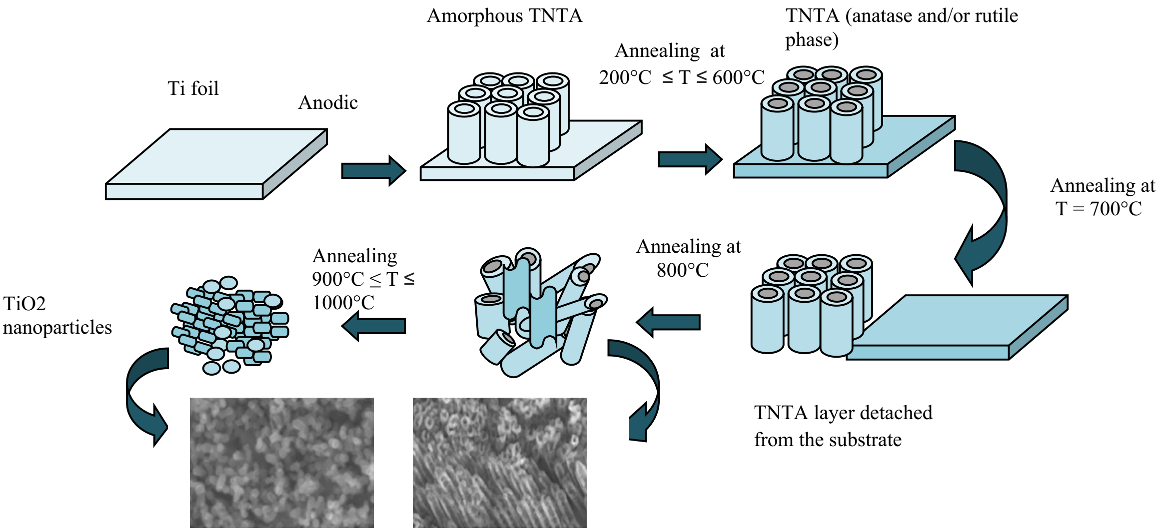

Scheme 1: The TiO_2 nanotubes fabrication procedure and the influence of temperature on their morphology.

in the literature that the anatase phase starts to create at 280 °C and the TiO_2 nanotubes thermally treated at 250 °C was amorphous and the full transformation to rutile phase occurred within 620° and 680 °C [65]. A similar behavior was also stated by several authors, and they suggested that the Ti is oxidized quickly and converted into rutile phase at high temperature [66,

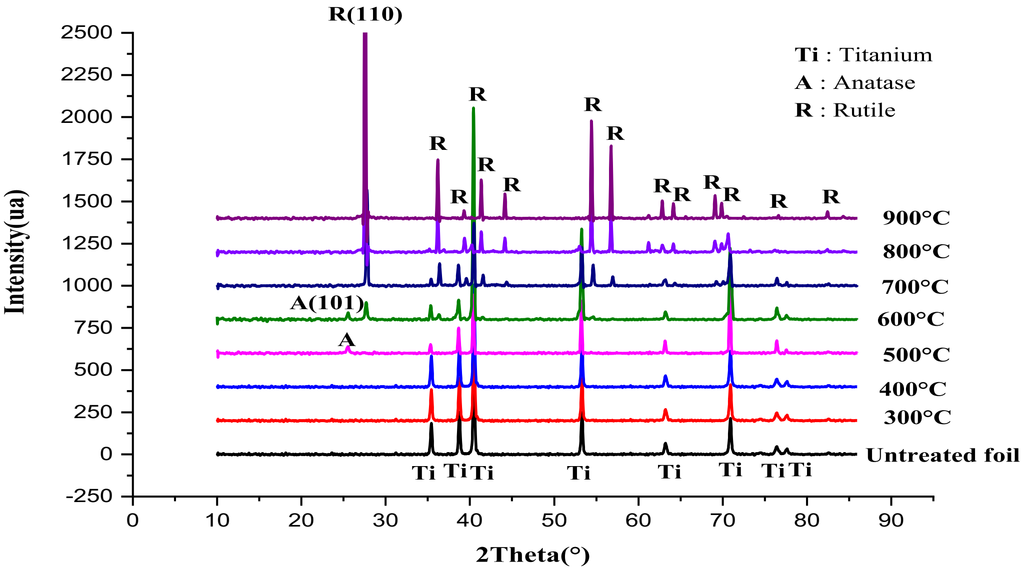

Figure 3: X-ray diffraction diffractograms of the as-prepared and thermally treated of TiO_2 nanotubes between 300 and 900 °C.

67]. Also, Gopal et al. [68] show that the nanotube stability is within the range of 550–600 °C. Since then, other works shown it is between 600 and 800 °C. This slight difference between the published results and also with our results is due to the difference in the experimental conditions, including the anodization parameters [68–72] and the duration of the heat treatment.

As can be observed in Fig. 3, the rise in the thermal treatment temperature from 600 to 900 °C gives rise to the increase in the intensity of the peaks of the rutile phase which is ascribed to the improvement in crystallinity.

The mean crystallite size could be calculated from the values of the full width at Half-Maximum (FWHM) of the diffraction peak of plan (110) using the Scherrer formula [73, 74]:

$$d = K.\frac{\lambda}{\beta cos\theta} \tag{1}$$

with d is the crystallite size in angstroms (Å), β is the broadening of the diffraction peak determined at half of its maximum intensity, λ is the X-ray wavelength (1.54060 Å), and θ is the diffraction angle.

The obtained value of crystallites size of anatase is 15.2 and 17.6 nm for the temperature of 500 and 600, respectively. For the rutile phase, the values of the crystallites sizes are 42.4, 53.4, 60.1, and 70.2 nm for the temperatures of 600, 700, 800, and 900 °C, respectively.

It can be seen clearly that the crystallite size of both anatase and rutile phases increases with thermal treatment temperature which is in agreement with the literature [75]. This behavior can be attributed to the collective fusion process of small grains into large grains, which becomes more accentuated for higher temperatures since they provide more energy to accelerate the growth of crystal grains [76]. This may also explain the increase in the rutile phase content with the calcination temperature.

Effect of annealing temperature on the optical properties of TiO2 nanotube

To determine the dependence of bandgap energy on temperature, we have investigate the diffuse reflectance spectroscopy of a TNT film annealed at different temperature. In Fig. 4, we present the diffuse reflectance measurements by varying the temperature from 300 to1000 °C and Kubelka–Munk function *F(R)* was applied to compute the direct energy bandgap, as given by Eq. (2) [77–79].

$$F(R) = \frac{(1-R)^2}{2R} \tag{2}$$

As one can observe that the nanotubes annealed at 600 °C present a lowest value of reflectivity of 7% in the visible region which is due to a better absorption of UV photons. This result is important as it can lead to generate more electron–hole pairs [80]. No oscillations (interference fringes) are observed for this sample, which can be related to a more homogenous chemical composition at 600 °C. Above this temperature, the intensity of the interference fringes also increases.

The band gap is one of the most important parameter of a material when it is being studied for opto-electrical applications. The optical tuning of the band gap to meet the specific requirements of a given application largely defines the effective use and suitability of the material for the application in question. We therefore studied the respective band gaps of anodized

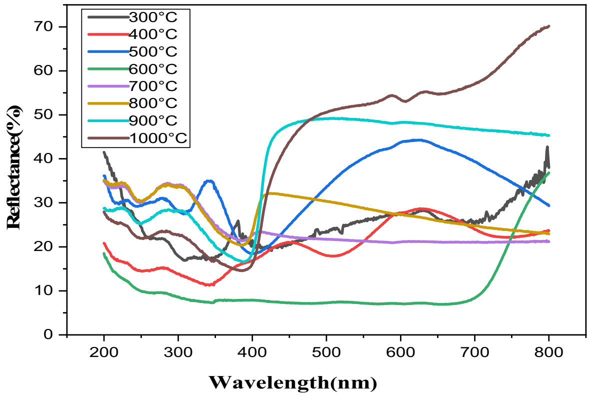

Figure 4: Diffuse reflectance of anodic TiO_2 nanotubes annealed at different temperature.

TABLE 1: Band gap value as a function of temperature deduced by Kubelka Munk plot.

Température (°C)	Gap (eV)
300	3.35
500	3.23
400	3.07
600	2.59
700	3.14
800	3.15
900	3.26
1000	3.11

and annealed samples and analyzed the corresponding changes as a function of the key experimental parameter (temperature).

Figure 6 displays $(F(R)\ h\nu)^2$ *vs.* hν diagram for TiO_2 nanotubes annealed at different temperatures. The direct energy band gap (Eg) can be evaluated by supposing a straight-line section of the $(F(R)\ h\nu)^2$ to pass across the hν axis.

The evaluated band gaps of anodized and annealed nanotubes are shown in Table 1 and Fig. 5 **s**hows the corresponding graph of this value.

The measured optical gap value (Table 1) decreases [81, 82] as the annealing temperature of the samples increases up to the temperature of 600 °C which corresponds to the lowest band gap value of 2.59 eV, resulting in a better energy absorption of the sample at this temperature. The remarkable decrease of the gap can be related to the presence of the mixed phase ($Ti–TiO_2(A)–TiO_2(R)$). In our knowledge [80–87] none of the works published in the literature has linked this strong decrease in the optical gap to the presence of the ($Ti–TiO_2(A)–TiO_2(R)$) phase, more precisely the presence of the Ti phase in the sample annealed at 600 °C. Beyond 600 °C the gap value increases again with increasing temperature and reaches the value of 3.26 eV at 900 °C which can be related to the disappearance of the Ti phase and the increase of the rutile portion.

At 1000 °C a decrease of the optical gap is observed again, which can be related to the decrease of the grain size.

Resistivity measurement

The electrical performance of device depends mainly on the used material resistivity in its fabrication. Therefore, it is important to know beforehand the electrical resistivity of the material. Among the methods used to measure this parameter is the four-point method. In this work, we used it to measure the sheet resistance of the prepared TiO_2 nanotubes and annealed at various temperatures.

The sheet resistance is the ratio of the voltage drop (V) measured between the two internal probes to the applied current (I) at two external probes multiplied by a geometric correction factor, according to the following equation:

$$R_s = K\left(\frac{V}{I}\right) \tag{3}$$

where R_s is the sheet resistance and k is a geometric factor which is 4.53 for a semi-infinite thin sheet. The resistivity of a layer is obtained multiplying the Rs by its thickness.

Figure 6 illustrates the change of the resistivity of layer of TiO_2 nanotubes determined by the four-point method as a function of thermal treatment temperature. Each resistivity value displayed in the figure is the average value and the estimated error is about 5×10^{-5} Ω.cm. It can be seen that the resistivity reduces from 95.23 to 29.56Ω.cm when the thermal treatment temperature increases from 200 to 800 °C, respectively. However, in the range of 500–600 °C, the resistivity decreases less quickly from 63.33 to 55.23 Ω.cm. The decrease in resistivity with the increases of thermal treatment temperature can be ascribed to increment in particle size which leads to a decrease in grain boundaries [88].

Electronic characterization (Mott-Schottky analysis)

Mott–Schottky analysis was extensively used to investigate and characterize the semiconductor material properties [89–91]. It consists to measure the variation of electrode capacitance (C) versus applied potential (E).The variation of the inverse of square capacitance (C) versus applied potential (E) is a straight line under depletion conditions. For an *n*- or *p*-type semiconductor, it is as follows [92, 93]:

$$\frac{1}{C_{SC}^2} = \frac{2}{e\varepsilon\varepsilon_o N_D}\left(\mathrm{E} - E_{FB} - \frac{KT}{e}\right)\text{for } n \text{ type semiconductor} \tag{4}$$

$$\frac{1}{C_{SC}^2} = -\frac{2}{e\varepsilon\varepsilon_o N_D}\left(E - E_{FB} - \frac{KT}{e}\right)\text{for } p \text{ type semiconductor} \tag{5}$$

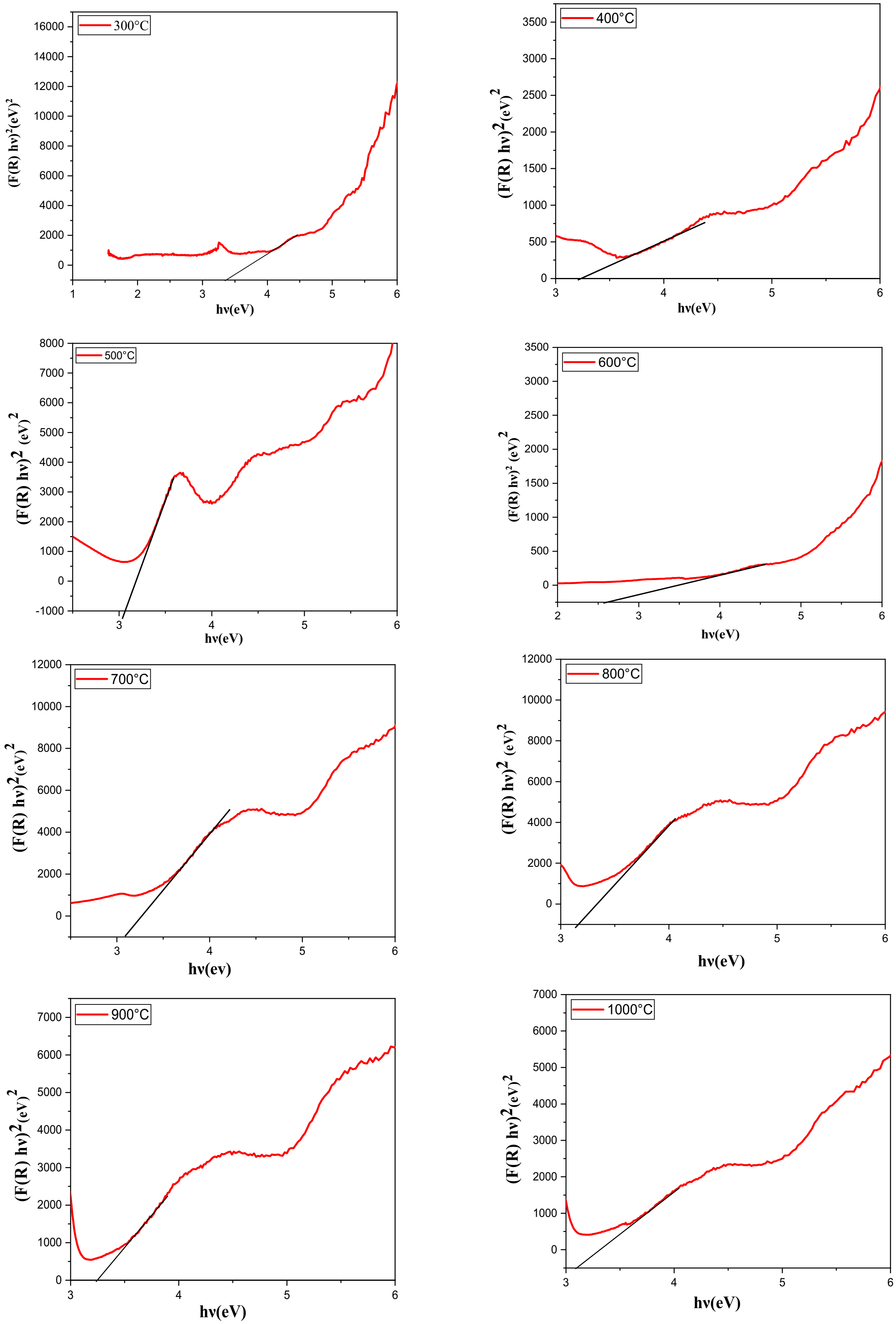

Figure 5: Kubelka Munk plot of the anodic TiO_2 nanotubes annealed at different temperatures.

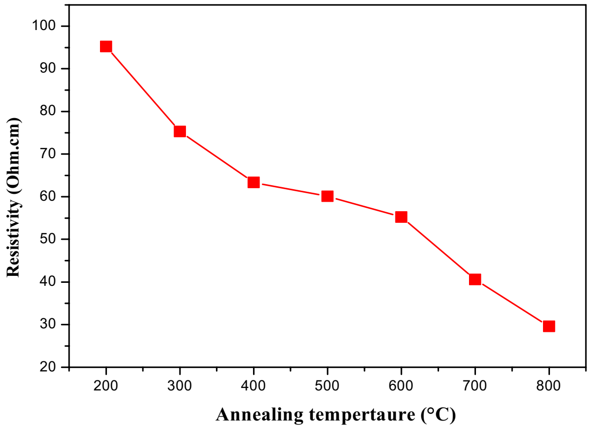

Figure 6: Dependence of the resistivity of the layer of TiO_2 nanotubes on annealing temperature.

where e is the charge of electron (– 1.602 10^{-19} C), N_D is the concentration of electron donor for an *n*-type semi-conductor or hole acceptor concentration for a *p*-type semi-conductor, ε is the dielectric constant of the passive film, ε_0(= 8.854 10^{-4} F/cm) is the vacuum permittivity, k(= 1.38 10^{-23} J/K) is the Boltzmann constant, *E* is the applied potential, T is the absolute temperature, and E_{FB} is the flatband. The term kT/e can be neglected because its value is just around 25 mV at room temperature.

In this study, the measurements were conducted in 0.05 M H_3BO_3-0.075 M $Na_2B_4O_7$–H_2O electrolyte in the potential range of – 1–0.8 V/SCE. Mott–Schottky curves were plotted by taking the values of the capacitance determined by impedance measurements at a frequency of 2 kHz and at various potentials [94]. A Mott-Schottky model, considering the morphology of nanotube arrays, was used to evidence the effect of temperature on carrier density (N_D) of TiO_2 nanotubes. The details of this model can be found elsewhere [95].

Figure 7 displays Mott–Schottky plots of TiO_2 nanotubes formed in ethylene glycol at 50 V for 2 h and annealed for 3 h at different temperatures: 200,300,400,500,600,700, and 800 °C. As it is difficult to discern the plots when they are together in the same figure, they are represented separately.

Overall, all Mott–Schottky plots display the same behavior but with different slopes and amplitudes. A linear variation of C^{-2}versus E can be seen in the range of 0.3–0.6 V/SCE for all plots. The slopes of these plot portions are positive, which is coherent with n-type semiconductor comportment. The appearance of a peak in Mott–Schottky plots [Fig. 7(f and g)] indicates the semiconductor type inverses from n-type to p-type when the applied voltage exceeds the peak value [94].

According to Eq. (3), the donor density can be determined from the slope of the $1/C^2$ *versus* E, and the flat band potential (E_{FB}) can be evaluated by extrapolation of the linear portion to $1/C^2 = 0$. A value of $\varepsilon = 120$ was used for the determination of N_D which is the average of several literature values [95–97]. It can see that the semiconducting properties of TiO_2 nanotubes are modified by the annealing temperature. The estimated values of the electron density (N_D) and flat band potential (E_{FB}) are listed in Table 2.

Table 2 shows the variation in the density of donors of TiO_2 nanotubes and flat band potential versus thermal treatment temperature. One can note that the density of donors decreases from 2. 34 10^{+21} to 3.61 10^{+13} cm^{-3} when the thermal treatment temperature rises from 200 to 800 °C, respectively [97]. Since the titanium interstitials and the oxygen vacancies are electron donors for TiO_2 [89–92], the decrease in charge carrier density can be ascribed to the reduction of defects present in the material [97]. However, the values of flatband potential (EFB) takes increasingly more negative values with increasing of annealing temperature: from– 0.22 V at 200 °C to – 0.61 V at 800 °C. This behavior may be due to the removal of species introduced into the layer of TiO_2 nanotubes during electrochemical anodization [98].

Conclusion

In summary, well-ordered TiO_2 nanotube arrays were synthesized by anodization of Ti in an aqueous solution of NH_4F and ethylene glycol at 50 V for 2 h. The influence of annealing temperature on the optical, morphological, structural, and electrical properties of the TiO_2 nanotube arrays was studied. It was noted that TiO_2 nanotube arrays present a low reflection of (7%) at 600 °C which corresponds to the lowest optical band gap value of 2.59 eV. It could subsist stably until at temperatures below 700 °C. More rising annealing temperature would lead to the collapse of nanotubes related to phase change from anatase to rutile and right from Ti to rutile, indicating the limiting thermal stability at this temperature. As the annealing temperature reaches to 900 °C, the whole nanotubes converted into the nanoparticles matrices.

The XRD diffractograms of the TiO_2 nanotubes showed that they are amorphous for annealing temperatures of 300 and 400 °C. Only the anatase phase was detected at the annealing temperature of 500 °C. The mixture of anatase and rutile phases was detected in the temperature range of 600–700 °C. Exceeding 700 °C, all TiO_2 nanotubes are converted in to single-phase of TiO_2 rutile. The change from amorphous-to-polycrystalline nature occurs after annealing at 500 °C. The samples thermally treated at 600 °C possess a mixture of phases (Ti–TiO2 anatase-TiO2 rutile). At this temperature, the correlation between the different properties has been reported, in fact, the nanotubes are intact and reveals improvement in absorption efficiency in the visible range with a very low value of the optical band gap of 2.59 eV, which is related to the presence of the mixed phase (Ti–TiO_2(A)–TiO_2(R)). This allows us to consider TiO2 nanotubes as photoanode used in optoelectronic components

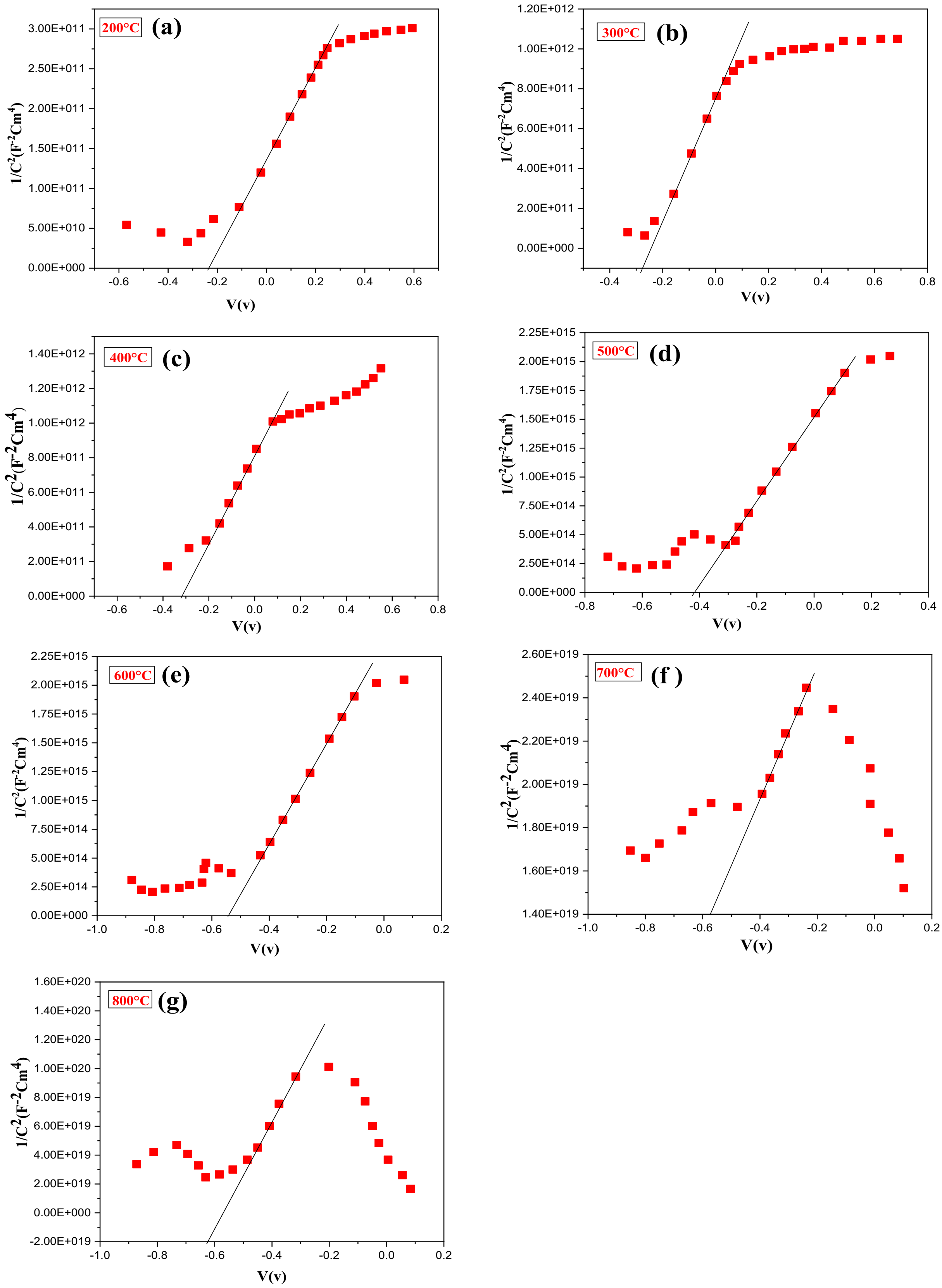

Figure 7: Mott–Schottky curves of TiO_2 nanotubes thermally treated at various temperatures as indicated in the figures. The analysis were performed using a borate buffer electrolyte.

TABLE 2: Semiconducting properties of oxide barrier films deduced from linear portions of the M–S plots of Fig. 7.

Annealing temperature (°C)	E_{FB} (V/SCE)	N_D (cm^{-3})
200	– 0.22	$2.34 \times 10^{+21}$
300	– 0.29	$4.02 \times 10^{+20}$
400	– 0.32	$5.91 \times 10^{+19}$
500	– 0.42	$5.70 \times 10^{+18}$
600	– 0.54	$2.03 \times 10^{+17}$
700	– 0.58	$4.63 \times 10^{+15}$
800	– 0.61	$3.61 \times 10^{+13}$

manufacturing and photocatalysis. After 700 °C, all the TiO_2 nanotubes are converted in to the single-phase of TiO_2 rutile.

The adjustment of annealing temperature can optimize the electrical performances of TiO_2 nanotubes. The thermal treatment effectively enhances the conductivity of TiO_2 nanotubes layers and reduces their resistivity due to the increase in particle size. Conductive TiO_2 nanotubes can improve the electron transport to external circuit, thus increase the efficiency of dye sensitized solar cells. Moreover, it was found that the electronic density is reduced with increasing annealing temperatures, from $2.34 \times 10^{+21}$ cm^{-3} at 300 °C to $3.61 \times 10^{+13}$ cm^{-3} at 900 °C which is related to the decrease of defects present in the material.

The elaborated TiO_2 NTs structures have a great potential for improving the performances of dye sensitized solar cells and other types of photovoltaic cells such as hybrid, organic–inorganic, or perovskite solar cells.

Experimental details

For the anodic growth of nanotubes, we used the titanium foils of 99, 7% purity and 1 mm of thickness. Moreover, to obtain mirror-like surface, we mechanically polished the titanium with abrasive Sic grains. After that, they were cleaned by sonication in acetone, ethanol, and deionized water for 15 min each, and then they were dried under a gentle stream of N_2.

TiO_2 nanotubes were obtained by anodization using a two-electrode setup cell. The Pt and a Ti foil (exposed area: 1 cm^2) were used as cathode and anode, respectively. A DC power source was used to apply a constant voltage of 50 V for 2 h between both electrodes.

The electrolyte used was composed of NH4F and Ethylene Glycol purchased from Sigma-Aldrich at room temperature (20 °C) [99–102]. The concentrations of deionized water and NH_4F were 3% and 0.3%, respectively. The distance between the two electrodes was set to about 1 cm. All samples of TiO_2 nanotubes were thermally annealed for 3 h under air environment in a tubular furnace. The annealing temperature range was 200–900 °C and the increase from room temperature to the annealing temperature was performed with a 5 °C/min heating rate.

The electronic properties of TiO_2 nanotubes were studied by the electrochemical impedance spectroscopy (EIS) using an Autolab PGSTAT-30 potentiostat/galvanostat driven by FRA 4.9 software, operating over the frequency range of 100 kHz—0.01 Hz. An ac voltage of amplitude 10 mV was applied to the working electrode. A classical cell with three electrodes was used; where a saturated calomel electrode (SCE), Pt plat, and anodized Ti foil were used as reference electrode, counter electrode, and working electrode, respectively. A borate buffer solution (0.05 M H_3BO_3-0.075 M $Na_2B_4O_7$–H_2O) with pH 9.2 was used as electrolyte.

All experiments were performed at room temperature (22 ± 2 °C), while the scan rate was of 1 mV/s in the range of 1–1.5 V. The prepared TiO_2 nanotubes were analyzed using various characterization techniques. X-ray diffraction (XRD) diffractograms were recorded using a Bruker D8 Advance X-ray diffractometer with CuKα ($\lambda = 1.54$ Å) radiation as the source over a 2θ range of 10–80°. The morphology of the prepared samples was examined with a SEM (XL30 ESEM), equipped with an EDX (energy dispersive X-ray spectroscopy), which was used to estimate the chemical composition. A UV–Visible spectrometer Evolution 220 is used for measuring the diffuse reflectance of our samples.

Acknowledgments

The authors gratefully acknowledge the financial support from General Direction of Scientific Research and Technological Development; Algeria (DGRSDT/MESRS).The authors thank Amirouche Saifi (University of Tizi-Ouzou) for SEM images.

Data availability

We declare the availability of the data presented in the text of the manuscript. All authors are aware of its content and have approved the manuscript and take full responsibility for its contents.

References

1. A. Kassam, W. Yuyin, B. Yang, S. Karthikeyan, L. Wei, New J. Chem. **46**, 15495–15503 (2022)
2. A. Raghavan, S. Sarkar, L.R. Nagappagari, L. Reddy, N.S. Bojja, S.M. Venkatakrishnan, S. Ghosh, Am. Chem. Soc. **59**, 13060–13068 (2020)
3. P.H. Nguyen, T.M. Cao, T.T. Nguyen, H.D. Tong, V.V. Pham, Beilstein J. Nanotechnol. **13**, 1541–1550 (2022)
4. A.J. Haider, Z.N. Jameel, I.H.M. Al-Hussaini, Energy Procedia **157**, 17–29 (2019)

5. W. Linlin, W. Liang, S. Yawei, Z. Bin, Z. Zhaohui, D. Guanghui, Z. Hongwei, Chemosphere **306**, 135628 (2022)
6. C. Mingjie, L. Yanping, D. Kexin, W. Chunchun, L. Shijie, J. Colloid Interface Sci. **629**, 276–286 (2023)
7. W. Chunchun, Y. Ruyu, C. Mingjie, L. Yanping, L. Shijie, Appl. Surf. Sci. **610**, 155346 (2023)
8. C. Mingjie, L. Yanping, W. Chunchun, L. Wei, L. Shijie, J. Sep. Purif. Technol. **304**, 122401 (2023)
9. C. Mingjie, W. Chunchun, L. Yanping, Y. Ruyu, L. Shijie, J. Sep. Purif. Technol. **300**, 121892 (2022)
10. L. Shijie, W. Chunchun, L. Yanping, L. Yazi, C. Mingjie, Z. Wei, D. Xiaoguang, J. Chem. Eng. **455**, 140943 (2023)
11. A.J. Frank, N. Kopidakis, J. Van de Lagemaat, Coord. Chem. Rev. **248**, 1165–1179 (2004)
12. S. Banerjee, S.K. Mohapatra, P.P. Das, M. Misra, J. Mater. Chem. **20**, 6784–6791 (2008)
13. Y. Hou, X.Y. Li, Q.D. Zhao, X. Quan, G.H. Chen, Adv. Func. Mater. **20**, 2165–2174 (2010)
14. S.Q. Liu, N. Zhang, Z.R. Tang, Y.J. Xu, ACS Appl. Mater. Interfaces. **4**, 6378–6385 (2012)
15. Y. Sun, K. Yan, G. Wang, W. Guo, T. Ma, J. Phys. Chem. C **115**, 12844–12849 (2011)
16. K. Zhu, N.R. Neale, A. Miedaner, A.J. Frank, Nano Lett. **7**, 69–74 (2007)
17. K. Shankar, J.I. Basham, N.K. Allam, O.K. Varghese, G.K. Mor, X.J. Feng, M. Paulose, J.A. Seabold, K. Choi, C.A. Grimes, J. Phys. Chem. C **113**, 6327–6359 (2009)
18. H. Tada, F. Suzuki, S. Ito, T. Akita, K. Tanaka, T. Kawahara, H. Kobayashi, J. Phys. Chem. B **106**, 8714–8720 (2002)
19. N.K. Allam, K. Shankar, C.A. Grimes, J. Mater. Chem. **18**, 2341–2348 (2008)
20. Y. Yue, P. Han, X. He, K. Zhang, Z. Liu, C. Zhang, S. Dong, L. Gu, G. Cui, J. Mater. Chem. **22**, 4938 (2012)
21. Y. Sorachon, H.E. Prakasam, O.K. Varghese, K. Shankar, M. Paulose, G.K. Mor, L.J. Thomas, C.A. Grimes, Nano Lett. **4**, 334–339 (2006)
22. G.K. Mor, M.A. Carvalho, O.K.M. Varghese, V. Pishko, C.A. Grimes, J. Mater. Res. **19**, 628–634 (2004)
23. R.N. Ghoshtagore, A.J. Noreika, J. Electrochem. Soc. **117**, 1310 (1970)
24. T. Fuyuki, H. Matsunami, Jpn. J. Appl. Phys. **25**, 1288 (1986)
25. N. Rausch, E.P. Butte, J. Electrochem. Soc. **140**, 145 (1993)
26. H. Cao, Z. Wang, G. Hou, G. Zheng, Surf. Coat. Technol. **205**, 885–889 (2010)
27. G.W. Dale, H.H. Fox, B.J.J. Zelinski, L. Weller-Brophy, Journal of Materials Research Society. Better Ceram. Through Chem. **5**, 371 (1990)
28. A. Elsaeed, M. Fattah, M. Dardir, Prog. Org. Coat. **78**, 83–89 (2015)
29. A. Jaroenworaluck, D. Regonini, C.R. Bowen, R. Stevens, J. Mater. Res. **23**, 2116 (2008)
30. A. Jaroenworaluck, D. Regonini, C.R. Bowen, R. Stevens, D. Allsopp, J. Mater. Sci. **42**, 6729 (2007)
31. O.K. Varghese, D. Gong, M. Paulose, C.A. Grimes, E.C. Dickey, J. Mater. Res. **18**, 156–165 (2003)
32. M. Jarosz, K. Syrek, J.K. Kolodziej, J. Mech, K. Malek, K. Hnida, T. Lojewski, M. Jaskula, G.D. Sulka, J. Phys. Chem. C **119**, 24182–24191 (2015)
33. S.J. Ku, G.C. Jo, C.H. Bak, S.M. Kim, Y.R. Shin, K.H. Kim, S.H. Kwon, J.-B. Kim, Nanotechnology **24**, 85301 (2013)
34. J.M. Macak, H. Tsuchiya, A. Ghicov, K. Yasuda, R. Hahn, S. Bauer, P. Schmuki, Curr. Opin. Solid State Mater. Sci. **11**, 3–18 (2007)
35. M. Li, X. Xiao, R. Liu, Appl. Surf. Sci. **255**, 365–367 (2008)
36. H. Li, L. Cao, W. Liu, G. Su, B. Dong, Ceram. Int. **38**, 5791–5797 (2012)
37. Y. Lai, C. Lin, H. Wang, J. Huang, H. Zhuang, L. Sun, Electrochem. Commun. **10**, 387–391 (2008)
38. R. Mohammadpour, A. Iraji zad, A. Hagfeldt, G. Boschloo, Phys. Chem. **13**, 21487–21491 (2011)
39. J. Hu, J. Cheng, S. Tong, L. Zhao, J. Duan, Y. Yang, J. Mater. Sci.: Mater. Electron. **27**, 5362–5370 (2016)
40. Y.H. Wu, Y.F. Cao, Z.Z. Fu, B.X. Lei, Z.F. Sun, Adv. Powder Technol. **32**, 186–193 (2021)
41. M.I. Khan, I. Shahnawaz, Y. Shahid, M.W. Waqas, A. Adil, F. Majeed, K. Shahbaz, M. Fiaz, A. Tariq, J. Nanoelectron. Optoelectron. **14**, 1582–2158 (2019)
42. S. Arshdeep, K. Sandeep, J. Alloy. Compd. **5**, 166709 (2022)
43. L. Wei, L. Fu, S. Ting, T. Xinyu, J. Lihua, X. Ting, X. Peng, Mater. Lett. **243**, 108–111 (2019)
44. A. Khlyustova, N. Sirotkin, T. Kusova, A. Kraev, V. Titov, A. Agafonov, Materials Advance **1**, 1193–1201 (2020)
45. P.S. Basavarajappa, S.B. Patil, N. Ganganagappa, K.R. Reddy, A.V. Raghu, C. VenkataReddy, Int. J. Hydr. Energy **45**, 7764–7778 (2020)
46. D. Zhang, J. Chen, Q. Xiang, Y. Li, M. Liu, Y. Liao, Am. Chem. Soc. **19**, 12511–12515 (2019)
47. P. Niu, G. Wu, P. Chen, H. Zheng, Q. Cao, H. Jiang, Front. Chem. **8**, 172 (2020)
48. F. Mohammadpour, M. Moradi, K. Lee, G. Cha, S. So, A. Kahnt, D.M. Guldi, M. Altomare, P. Schmuki, Chem. Commun. **51**, 1631–1634 (2015)
49. K. Zhu, N.R. Neale, A.F. Halverson, J.Y. Kim, A.J. Frank, J. Phys. Chim. **114**, 13433–13441 (2010)
50. J. Lin, M. Guo, C.T. Yip, W. Lu, G. Zhang, X. Liu, X. Chen, H. Huan, Adv. Funct. Mater. **23**, 5952–5960 (2013)
51. A. Jaroenworaluck, D. Regonini, C.R. Bowen, R. Stevens, Appl. Surf. Sci. **256**, 2672–2677 (2010)
52. V.V. Pham, D.P. Duong, D.P. Bui, L.V. Hieu, M.T. Cao, Superlattices Microstruct. **117**, 305–316 (2018)
53. H. Li, J. Qu, Q. Cui, H. Xu, H. Luo, M. Chi, R.A. Meisner, W. Wang, D. Sheng, J. Mater. Chem. **21**, 9487 (2011)

54. N. Liu, K. Lee, P. Schmuki, Angew, Chemie - Int. Ed. **52**, 12381–12384 (2013)
55. D. Fang, Z. Luo, K. Huang, D.C. Lagoudas, Appl. Surf. Sci. **257**, 6451–6461 (2011)
56. A. Changzhi, X. Pengcheng, Z. Xidong, Z. Xusheng, L. Jin, K. Andreas, L. Shiwei, ACS Sustain. Chem. Eng. **7**, 5274–5282 (2019)
57. S. Anish, B. Susmita, B. Amit, Appl. Surf. Sci. **317**, 573–580 (2014)
58. R. Beranek, H. Tsuchiya, T. Sugishima, J.M. Macak, L. Taviera, S. Fujimoto, H. Kisch, P. Schmuki, Appl. Phys. Lett. **87**, 243114–243116 (2005)
59. H. Tsuchiya, J.M. Macak, A. Ghicov, A.S. Rader, L. Taveira, P. Schmuki, Corros. Sci. **49**, 203–210 (2007)
60. D. Regonini, A. Jaroenworaluck, R. Stevens, C.R. Bowen, Surface Interface Anal. **42**, 139–144 (2010)
61. J.M. Macak, S. Aldabergerova, A. Ghicov, P. Schmuki, Phys. Status Solidi **203**, 67–69 (2006)
62. A. Ghicov, H. Tsuchiya, J.M. Macak, P. Schmuki, Phys. Status Solidi **203**, 28–30 (2006)
63. A. Tighineanu, S.P. Albu, P. Schmuki, Phys. Status Solidi **8**, 158–164 (2014)
64. A. Tighineanu, T. Ruff, S.P. Albu, R. Hahn, P. Schmuki, Chem. Phys. Lett. **494**, 260–263 (2010)
65. W. Yang, Q. Peng, R. Chen, Y. Wen, B. Shan, Phys. Procedia **48**, 220–227 (2013)
66. O.K. Varghese, D.W. Gong, M. Paulose, C.A. Grimes, E.C. Dickey, J. Mater. Res. **18**, 156–165 (2003)
67. Y. Lei, Z. Miao, S. Shiwei, L. Jianguo, S. Xueping, H. Gang, S. Zhaoqi, Nanoscale Res. Lett. **9**, 621 (2014)
68. G.K. Mor, O.K. Varghese, M. Paulose, K. Shankar, C.A. Grimes, Sol. Energy Mater. Sol. Cells **90**, 2011–2075 (2006)
69. G.K. Mor, K.O. Varghese, M. Paulose, K. Shankar, C.A. Grimes, Solar Energy Mater. **9**, 2011–2075 (2006)
70. C. Dumitriu, C. Pîrvu, UPB Scientific Bulletin. Series B **3**, 74 (2012)
71. D. Regonini, A. Jaroenworaluck, R. Stevens, C.R. Bowen, Surf. Interface Anal. **42**, 139–144 (2010)
72. M.Y. Lan, C.P. Liu, H.H. Huang, J.K. Chang, S.W. Lee, Nanoscale Res. Lett. **8**, 150 (2013)
73. C.C. Koch, A. Ilya, O. Vidko, S. Sudipta, V. Stan, J. German, Chim. Soc. **47**, 2340–2342 (2008)
74. A. Monshi, M.F. Reza, M.M. Reza, WJNSE **2**, 154–160 (2012)
75. O. Harizanov, A. Harizanova, Sol. Energy Mater. Sol. Cells **63**, 185 (2000)
76. Y. Sun, E.D. Liu, L. Zhu, Y. Wen, Q.W. Tan, W. Feng, J. Nanomater. Biostruct. **14**, 463–470 (2019)
77. K.M. Chahrour, F.K. Yam, R. Abdalrheem, Mater. Lett. **248**, 161–164 (2019)
78. M. Pal, U. Pal, Y. Justo, M. Gracia, F. Jiménez, P. Rodríguez, Nanoscale Res. Lett. **7**, 1–12 (2012)
79. L. Shijie, C. Mingjie, L. Yanping, W. Chunchun, Y. Ruyu, C. Xiaobo, Adv. Powder Mater. **2**, 100073 (2023)
80. M. Chahrour, F.K. Yam, H.S. Lim, R. Abdalrheem, J. Phys: Conf. Ser. **1535**, 012012 (2020)
81. A.H. Abdulsada, A.K. Mishjil, N. Ahmad, IOP Conf. Series: J. Phys.: Conf. Series **1032**, 012037 (2018)
82. S. Das, R. Zazpe, J. Prikryl, P. Knotek, M. Krbal, H. Sopha, V. Podzemna, J.M. Macak, Electrochim. Acta **20**, 452–459 (2016)
83. A. Jesum, C. Fernandes, E. Kohlrausch, C. SherdilKhan, R. Brito, J.M. Guilherme, R.S. Teixeira, D. Jairton, J.M.L. Santos, J. Solid State Chem. **316**, 04–25 (2017)
84. G. Li, Z.Q. Liu, J. Lu, L. Wang, Z. Zhang, J. Appl. Surface Sci. **255**, 7323–7328 (2009)
85. Z. Lockman, C.H. Kit, S. Sreekantan, Special Ed. **6**, 1–07 (2009)
86. J. Yu, B. Wang, J. Appl. Catal. B: Environ. **94**, 295–302 (2010)
87. Y.C. Lim, Z. Zainal, M.Z. Hussein, W.T. Tan, J. Nanomater. Biostruct. **8**, 167–176 (2013)
88. M.I. Khan, S.I. Shahnawaz, M. Saleem, U.R. Saif, Results Phys. **8**, 249–252 (2018)
89. V.A Myamlin, Y.V.Pleskov, Plenum Press, New York, (1967).
90. SR.Morrison, Plenum Press, New York. (1980).
91. A.J. Nozik, R. Memming, J. Phys. Chem. **100**, 13061 (1996)
92. D.D. Macdonald, A. Sun, Electrochimical Acta **51**, 1767–1779 (2006)
93. P. Pu, H. Cachet, E.M.M. Sutter, Electrochim. Acta **55**, 5938 (2010)
94. A.A. Fattah, M.A. Golozar, A. Saatchi, K. Raeissi, Corros. Sci. **52**, 205–209 (2010)
95. J.F. McAleer, L.M. Peter, Faraday Discuss Am. Chem. Soc. **70**, 67 (1980)
96. K.E. Allard, M. Ahrens, K.E. Heusler, Werkst Corros **26**, 694 (1975)
97. F. Msuers, H.J. Tolle, R. Memming, J. Electrochem. Soc. **121**, 1160 (1974)
98. A.P. Prospero, C.C.J. Edgar, F. Gonzalez, G. Ignacio, Electrochim. Acta **06**, 056 (2014)
99. D. Regonini, A. Jaroenworaluck, R. Stevens, C.R. Bowen, Surface Interface Anal. **42**, 139–141 (2010)
100. M. Paulose, L. Peng, K.C. Popat, O.K. Varghese, T.J. Latempa, N.Z. Bao, A.G. Tejal, J. Craig, Membr. Sci. **319**, 199–205 (2008)
101. K. Kant, D. Losic, Physica Status Solid **3**, 139–141 (2009)
102. D. Losic, M. Lillo, J.D. Losic, Small **5**, 1392–1397 (2009)